Integrated Arctic Observation System

Research and Innovation Action under EC Horizon2020
Grant Agreement no. 727890

Project coordinator:
Nansen Environmental and Remote Sensing Center, Norway

Deliverable 2.8

Report on exploitation of existing data: Land and cryosphere

Start date of project:	01 December 2016	Duration:	60 months
Due date of deliverable:	31 May 2018	Actual submission date:	29 May 2018
Lead beneficiary for preparing the deliverable:	GEUS		
Person-months used to produce deliverable:	18.3 pm		

Authors: Andreas P. Ahlstrøm (GEUS), Roberta Pirazzini (FMI), David Gustafsson (SMHI), Kristina Isberg (SMHI), S. Abbas Khan (DTU), Francisco Navarro (UPM), Jaime Otero (UPM), Anne M. Solgaard (GEUS), Mathilde Sørensen (UiB), Peter Voss (GEUS), Tine B. Larsen (GEUS), Trine Dahl-Jensen (GEUS) Dariusz Ignatiuk (U Slaski), Małgorzata Błaszczyk (U Slaski), Mariusz Grabiec (U SlaskiI), Katrin Kohnert (GFZ), Andrei Serafimovich (GFZ), Torsten Sachs (GFZ), Anna Kontu (FMI), Tomasz Wawrzyniak (IGPAN), Piotr Glowacki (IGPAN)

Version	DATE	CHANGE RECORDS	LEAD AUTHOR
1.0	30/04/2017	Template	Roberta Pirazzini
1.1	14/12/2017	1st Draft	Roberta Pirazzini
2	28/05/2018	Final version	Andreas Ahlstrøm
2.1	29/05/2018	Minor edits of the lay-out	K. Lygre

Approval	Date:	Sign.
X	30.05.2018	*Skui Sandven* Coordinator

USED PERSON-MONTHS FOR THIS DELIVERABLE					
No	*Beneficiary*	*PM*	*No*	*Beneficiary*	*PM*
1	NERSC		24	Terradue	
2	UiB	*1*	25	GINR	
3	IMR		26	UNEXE	
4	MISU		27	NIVA	
5	AWI		28	CNRS	
6	IOPAN		29	U Helsinki	
7	DTU	*6*	30	GFZ	*4*
8	AU		31	ARMINE	
9	GEUS	*0.9*	32	IGPAN	*0.5*
10	FMI	*3.8*	33	U SLASKI	*0.6*
11	UNIS		34	BSC	
12	NORDECO		35	DNV GL	
13	SMHI	*1.5*	36	RIHMI-WDC	
14	USFD		37	NIERSC	
15	NUIM		38	WHOI	
16	IFREMER		39	SIO	
17	MPG		40	UAF	
18	EUROGOOS		41	U Laval	
19	EUROCEAN		42	ONC	
20	UPM	4	43	NMEFC	
21	UB		44	RADI	
22	UHAM		45	KOPRI	
23	NORUT		46	NIPR	
			47	PRIC	

DISSEMINATION LEVEL		
PU	Public, fully open	X
CO	Confidential, restricted under conditions set out in Model Grant Agreement	
CI	Classified, information as referred to in Commission Decision 2001/844/EC	

EXECUTIVE SUMMARY

This report presents higher-level products from existing terrestrial and cryosphere measurements, developed within INTAROS WP2 by applying new methodologies for data processing and derivation of new quantities. The report presents both satellite-derived products and products from in situ observing systems within the terrestrial sphere and the cryosphere.

The exploited higher-level products described in this report are evaluated with respect to requirements, capacities and gaps and recommendations in the companion report D2.7.

Table of Contents

1. Introduction

This report will present higher-level products from existing terrestrial and cryosphere measurements, developed within INTAROS WP2 by applying new methodologies for data processing and derivation of new quantities. The report will present both satellite-derived products and products from in situ observing systems within the terrestrial sphere and the cryosphere.

To avoid unnecessary repetition and to facilitate comparison and co-evaluation with un-exploited datasets and products, the exploited higher-level products described in this report are evaluated with respect to requirements, capacities and gaps and recommendations in the companion report D2.7.

This report thus only provides the descriptions of the higher-level products, while the properties of these are presented in D2.7.

This deliverable (D2.8) covers the data exploitation done on terrestrial and cryospheric data. Corresponding work on ocean and sea ice data, and atmospheric data is presented in deliverables D2.2 and D2.5, respectively.

2. Data exploitation

2.1 UiB and GEUS: Earthquake and focal mechanism catalog of the Arctic

As a contribution to D2.8 and D2.9, an earthquake catalog is developed for the Arctic region, including new focal mechanism solutions for the larger events. The catalog covers the area north of the Arctic Circle (65.563N) and include events with magnitude 3.5 or larger in the 50-year period 196501 – 201412 (2014 is the last full year reviewed by the ISC). A complete and homogeneous earthquake catalog is a prerequisite for studying seismic hazard and temporal variation in seismicity. The derived catalog will in this regard serve as a baseline for studying changes in seismicity rates associated with long-term climatic changes.

The catalog is based on all available earthquake catalogs covering at least parts of the Arctic. The location and magnitude of each event is chosen from the catalog which is considered most reliable at the time and location of the event. Available catalogs covering the Arctic region are presented in Table 1 with detailed information on data coverage and availability. The seismicity, as available in the ISC database, is presented in Figure 1 (International Seismological Centre, 2018). The final catalog will be presented in D2.9.

Existing moment tensor solutions have been downloaded from the Global CMT catalog (http://www.globalcmt.org Ekström at al., 2012). 391 solutions are currently available as presented in Figure 2. This dataset will be extended with a series of new focal mechanisms and (if possible) moment tensor solutions for events covered by the NNSN and GLISN networks. The new and improved catalog, including focal mechanisms, will be presented in D2.9.
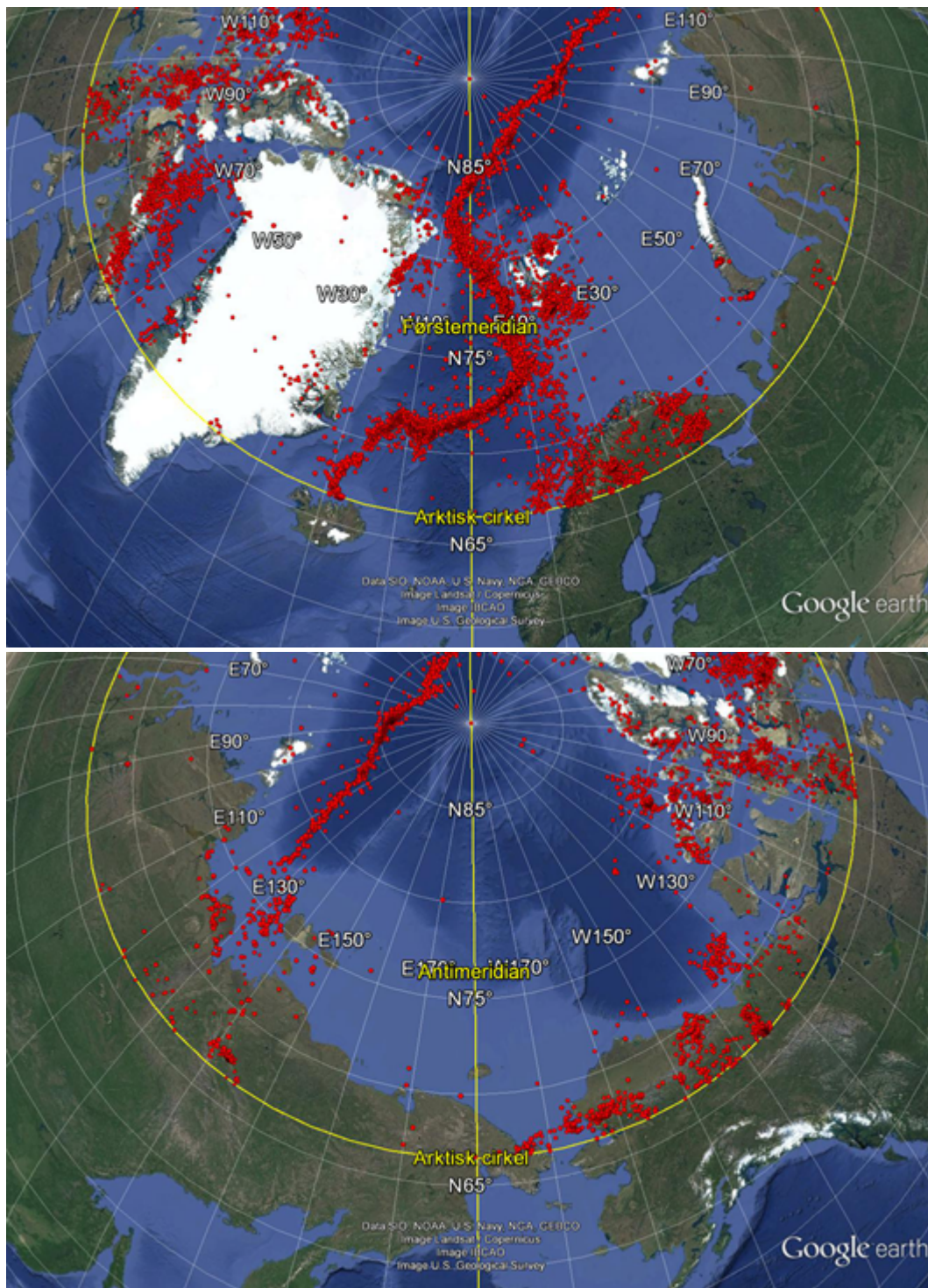
Figure 1: Seismic activity in the Arctic region in the time period 1965-2014 available in the ISC database. View from the meridian (upper panel) and antimeridian (lower panel).
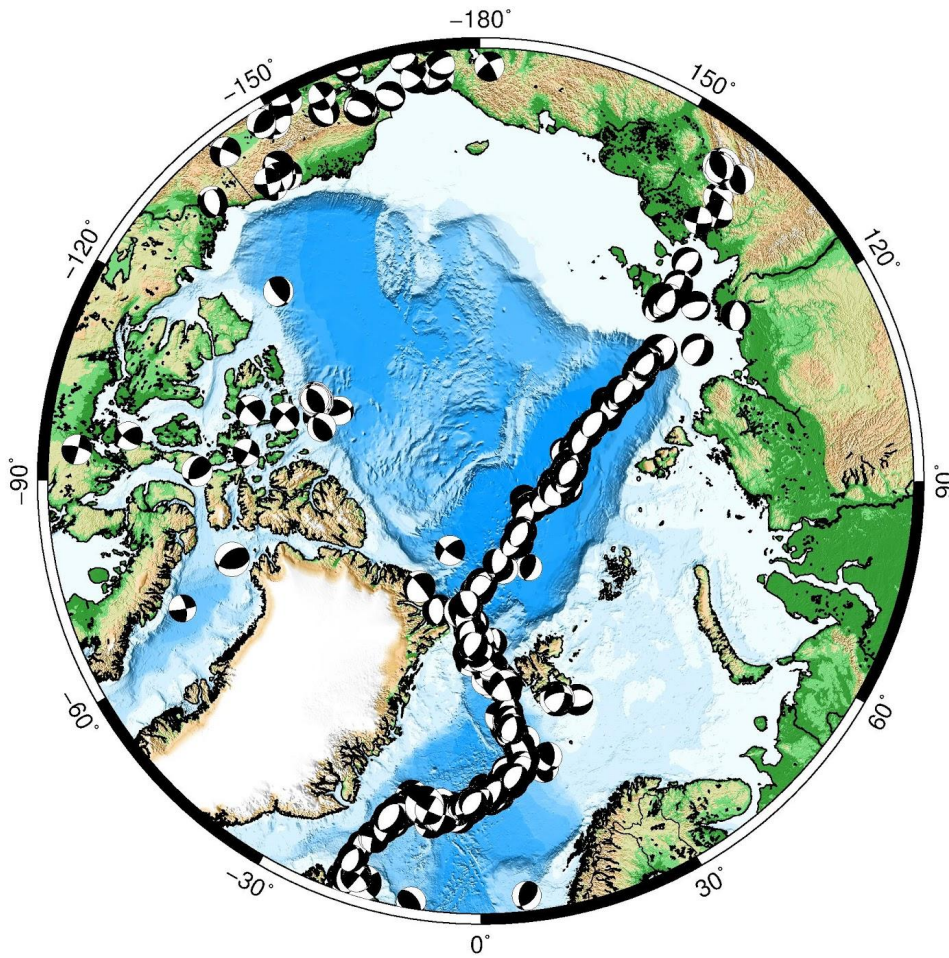
Figure 2: Moment tensor solutions available for the time period 1965 – 2014 in the Global CMT catalog (www.globalcmt.org).

No.	Institution	Country	Name	URL	Period	Region	Catalogue URL	Note
1	Institute of Volcanology and Seismology, Far Eastern Branch of the Russian Academy of Sciences (FEB RAS), Petropavlovsk-Kamchatsky, Russia	RU	Database "Earthquakes of the Northern Group of Volcanoes of Kamchatka 1971-1996."	http://geoportal.kscnet.ru/geonetwork/srv/eng/catalog.search#/metadata/27f1e2c9-f3c9-49c1-b1f3-87ea280a439d	1971-1996	Kamchatka	http://geoportal.kscnet.ru/seismo/NewFormSelect.php	Download of the catalogue doesn't work
2	Incorporated Research Institutions for Seismology (IRIS), Washington, USA	USA	IRIS Earthquake Browser	https://ds.iris.edu/ieb	1970-present	World		Web interface
3	US Gological Survey (USGS)	USA	Composite regional catalogs of earthquakes in the former Soviet Union	https://earthquake.usgs.gov/data/russia_seismicity/	1955-2002	Russia	https://pubs.usgs.gov/of/2002/0500/report.pdf	Open File Report. Comprehensive compilation, documentation and evaluation of catalogs of seismicity of the former Soviet Union. These include four principal, Soviet-published catalog sources, supplemented by other publications. Contains list of Russian catalogues: Obninsk Bulletin (1955-1999), "Annual catalogues" (since 1992), "General Catalogue" and "New Cataloge" (compiled 1974). Covers Arctic Region (from p.32).
4	University of Alaska Fairbanks	USA	AEIC Earthquake Database	https://earthquake.alaska.edu/	1898-present (?)	Alaska	http://www.aeic.alaska.edu/html_docs/db2catalog.html	They have seismic network as well. Catalogue downloadable via FTP after request.
5	Institute of Physics of the Earth. O.Yu. Schmidt of the RAS, Moscow, Russia	RU	territory (0 ° - 70 ° N, -20 ° W - 180 ° E)	http://www.ifz.ru/open_data/	1981-2012	Russia		3 catalogues: Mostryukov AO, Petrov VA Catalog of mechanisms of earthquake foci according to literature data; Catalog of mechanisms of foci for 1981 - 2012 gg.; Focal Mechanisms; territory (0 ° - 70 ° N, -20 ° W - 180 ° E)

6	Natural Resources Canada	CA	Earthquake Database	http://www.earthquakescanada.nrcan.gc.ca/stndon/NEDB-BNDS/index-en.php	1985-present	Canada	http://www.earthquakescanada.nrcan.gc.ca/stndon/NEDB-BNDS/bull-en.php	Web interface. The database contains nearly 85,000 earthquakes in or near Canada and nearly 19,000 mining-related events, mining and construction blasts, and other induced events between 1985-2015. 2276 EQs above 70deg N. KMZ files available.
7	Natural Resources Canada	CA	Seismic Hazard Earthquake Epicentre File (SHEEF) used in the fourth generation seismic hazard maps of Canada	http://geopub.nrcan.gc.ca/register_e.php?id=261333	1627-2008	Canada		Open file, which contains all earthquakes from the database in or near Canada with a magnitude of 2.5 and greater for the time period of 1627 to 2008. It can be downloaded from the GeoPub website
8	World Data Center for Marine Geology and Geophysics	USA (RU)	Seismically active zones of the arctic (G.P.Avetisov,Saint Petersburg, VNIIOkeangeologia, 1996)	https://www.ngdc.noaa.gov/mgg/avetisov/avetisov.htm	1969-1988	Arctic (Russia)	https://www.ngdc.noaa.gov/mgg/avetisov/Appendix.htm	Catalogue of the epicenters of the earthquakes registrated by SEVMORGEO stations. This publication is offered by the World Data Center for Marine Geology and Geophysics, Boulder with the permission of the authors. It is a translation and update of a work previously published only in Russian. 158 EQs, location accuracy 5-50km.
9	GEOLOGICAL SURVEY OF DENMARK AND GREENLAND (GEUS), DK	DK	Seismic Services	http://www.geus.dk/DK/nature-climate/natural-disasters/seismology/Sider/default.aspx	1926-present	Denmark + Greenland	http://www.geus.dk/DK/nature-climate/natural-disasters/seismology/Sider/seismo_reg-dk.aspx	All locations available via ISC.
10	International Seismological Centre, UK	UK	ISC Bulletin	http://www.isc.ac.uk/iscbulletin/	1900-present	World	http://www.isc.ac.uk/iscbulletin/search/catalogue/	Web interface. The ISC Bulletin contains data from 1900 to present day (2018-02-19). The Reviewed ISC Bulletin, which is manually checked by ISC analysts and relocated (when there are sufficient data) is typically 24 months behind real-time and is currently up to 2015-03-01.

11	Norwegian National Seismic Network (NNSN), University of Bergen + NORSAR, NO	NO	NNSN Catalogue	http://nnsn.geo.uib.no/	1900-present	Norway	ftp://ftp.geo.uib.no/pub/seismo/DATA/PARAMETRIC/	Parametric data in Nordic format, not bulletins.
12	Swedish National Seismic Network (SNSN), Uppsala University, SE	SE	Observations séismographiques & Seismological Bulletin	http://www.snsn.se/	1904-1998	Sweden	http://www.axelhamberg.se/Bulletin/Engelsk.htm	Scanned publications from Uppsala University, with data from seismological records from the years 1904-1998
13	Swedish National Seismic Network (SNSN), Uppsala University, SE	SE	Nordic Catalogues	http://www.snsn.se/	2000-present	Sweden	http://www.snsn.se/data/lists/nordic/	Links to event detections from Denmark, EMSC, Finland and Norway updated with readings from SNSN.
14	Institute of Seismology, University of Helsinki, FI	FI	Catalog of earthquakes in Northern Europe 1375-	http://www.seismo.helsinki.fi/english/bulletins/	1375-2012	Northern Europe	http://www.seismo.helsinki.fi/english/bulletins/catalog_northeurope.html	Various bulletins available: Catalog of earthquakes in Northern Europe 1375-; Catalog of earthquakes in Finland since 2000 (in Finnish); Catalog of earthquakes in Finland 1610 - 1999
15	European-Mediterranean Seismological Centre, FR	FR	Euro-Med Bulletin	https://www.emsc-csem.org/Bulletin/	1998-2012	Europe	https://www.emsc-csem.org/Earthquake/?filter=yes	Web interface
16	GEOFON, GFZ Potsdam, DE	DE	GEOFON Earthquake Information Service	https://geofon.gfz-potsdam.de/eqinfo/eqinfo.php	1980-present	World	https://geofon.gfz-potsdam.de/eqinfo/form.php?latmin=66&nmax=1000	Web interface. First EQs from Arctic region (lat >= 66 deg) from 2003, 633 events (2003 - 2018-02-20). Ther real-time bulletin is a product of the GEOFON Extended Virtual Network (GEVN).

17	International Data Centre (IDC), Comprehensive Nuclear-Test-Ban Treaty Organization (CTBTO), Vienna, AT	AT	International Data Centre product	https://www.ctbto.org/index.php?id=280&no_cache=1&letter=i#international-data-centre	?	World ?	?	Print outs of seismological, infrasound and hydroacoustic events, as well as the presence of radionuclides and noble gases in the atmosphere detected through evaluation of International Monitoring System (IMS) transmitted data. From automatic processing, lists of events emerge and, as events accumulate, they are made available to Member States. There are 3 levels of Standard Event Lists (SEL). The confirmed and corrected events are listed in the Reviewed Event Bulletin (REB) - from SEL3.
18	Lamont-Doherty Earth Observatory (LDEO), Columbia University	USA	Global Centroid Moment Tensor database (Harward CMT)	http://www.globalcmt.org/	1976-present	World	http://www.globalcmt.org/CMTsearch.html	442 events in Arctic region
19	GEOSCOPE Observatory, IPGP, FR	FR	Earthquake Catalogues	http://geoscope.ipgp.fr/index.php/en/	2006-present	World	http://geoscope.ipgp.fr/index.php/en/data/earthquake-data/catalogs-of-earthquakes	Yearly catalogues as ASCII files.

Table 1: [Starting on page 6] Earthquake catalogs including events in the Arctic region.

2.2 DTU: Ice mass change of the Greenland ice sheet from GRACE and GNET data

Geodetic methods used to determine ice sheet volume or mass changes include airborne and satellite radar and laser altimetry (surface elevation change method), observations of ice flow of outlet glaciers using satellite interferometric synthetic-aperture radar (InSAR) (which, when combined with SMB model output, is referred to as the Input-Output method), and measurements by the Gravity Recovery and Climate Experiment (GRACE) satellite mission of changes in the gravity field caused by changes in ice sheet mass (gravimetry method). All of these methods have characteristic advantages and disadvantages.   For example, airborne and satellite radar and laser altimetry have better spatial resolution than the GRACE observations, but they lack the high temporal resolution provided by the latter. Airborne and satellite radar and laser require assumptions about the firn density to convert volume to mass. In addition, satellite radar altimetry does not provide reliable results in regions of large slopes, such as those along much of the GrIS margins, and is affected by radar penetration into the snow. The Input-Output method provides the best understanding of the underlying cause of mass change in a region, but it requires knowledge of such things as outlet glacier depths, and only measures velocity along the line of site, which is problematic in many areas. Furthermore, since the net mass variations obtained using the Input-Output method are the differences between two large and, in most cases, nearly equal numbers (i.e. an SMB estimate, and an InSAR-based discharge estimate), relatively small errors in either of those numbers can lead to a relatively large error in the net mass balance. The gravimetry method provides direct estimates of mass, but has limited resolution (>250 km) and is affected by mass changes not just from ice and snow variations, but also from hydrologic and ocean mass changes, and from mass variations in the underlying solid Earth, (especially, glacial isostatic adjustment, GIA).

However, combining GRACE and GNET data (see Fig. 3) can improve the resolution of ice sheet mass change (of 250 km from GRACE alone) to somewhat ~150 km or better. Fig. 3 shows the course 250 km grid resolution of GRACE and the location of GNET GPS data. GPS stations are mostly sensitively of local mass loss within ~70 km (yellow circle in Fig. 3) from the station. By merging GNET and GRACE data, mass loss from GRACE can be "relocated" to fit observed uplift (due to unloading of the earth crust).

Improves mass change is possible from 2007-present, as the full constellation of GNET was established in 2007. Prior to 2007, only 14 stations were active, reducing the possibility of "relocating" ice mass change from GRACE.
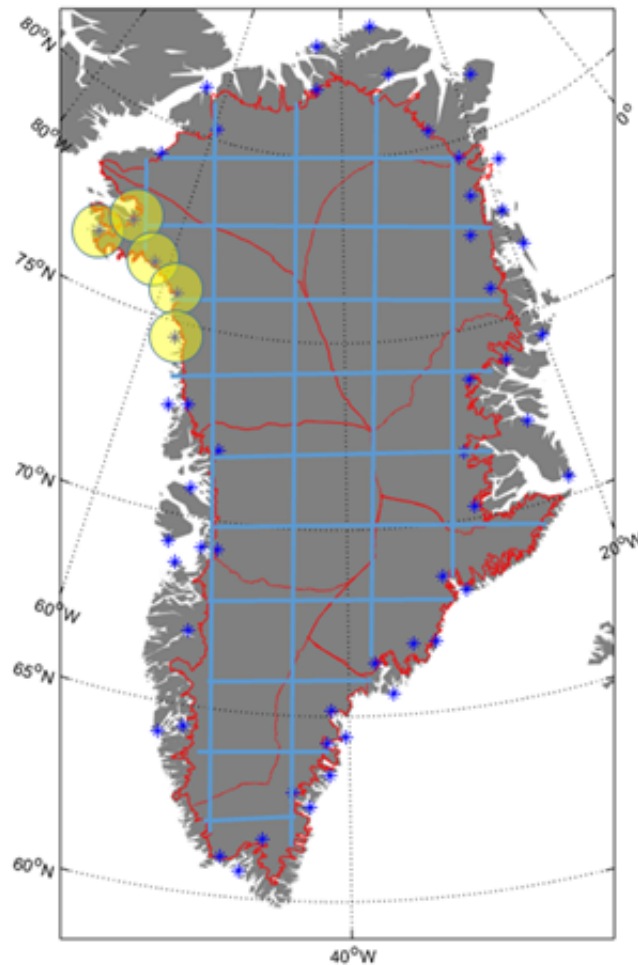
Figure 3: Resolution of GRACE mass change grids and location of GNET stations.

2.3   GEUS: Ice velocity maps of the Greenland ice sheet margin based on Sentinel-1 data

This dataset contains maps of ice velocity of the Greenland ice sheet margin based on ESA Sentinel-1 synthetic aperture radar (SAR) C-band data.

The operational interferometric post processing (IPP) chain [Dall et al., 2015], developed at the Technical University of Denmark (DTU) Space and upgraded with offset tracking for ESA's Climate Change Initiative (CCI) Greenland project, was employed to derive the surface movement using offset tracking [Strozzi et al., 2002]. The IPP uses a pair of SAR images covering the same area and calculates the spatially varying offsets between the two by determining the cross-correlation between image patches. The three-dimensional velocity vectors are then determined by assuming surface-parallel flow using surface-elevation data for Greenland from the GIMP-project (Howat et al., 2014; 2015). The data are provided on a polar stereographic grid (EPSG3413: Latitude of true scale 70N, Reference Longitude 45E). The horizontal velocity is provided in true meters per day, towards EASTING (x) and NORTHING

(y) direction of the grid, and the vertical displacement (z) is provided along with the error standard deviations for each component. The spatial resolution is 500x500 m.
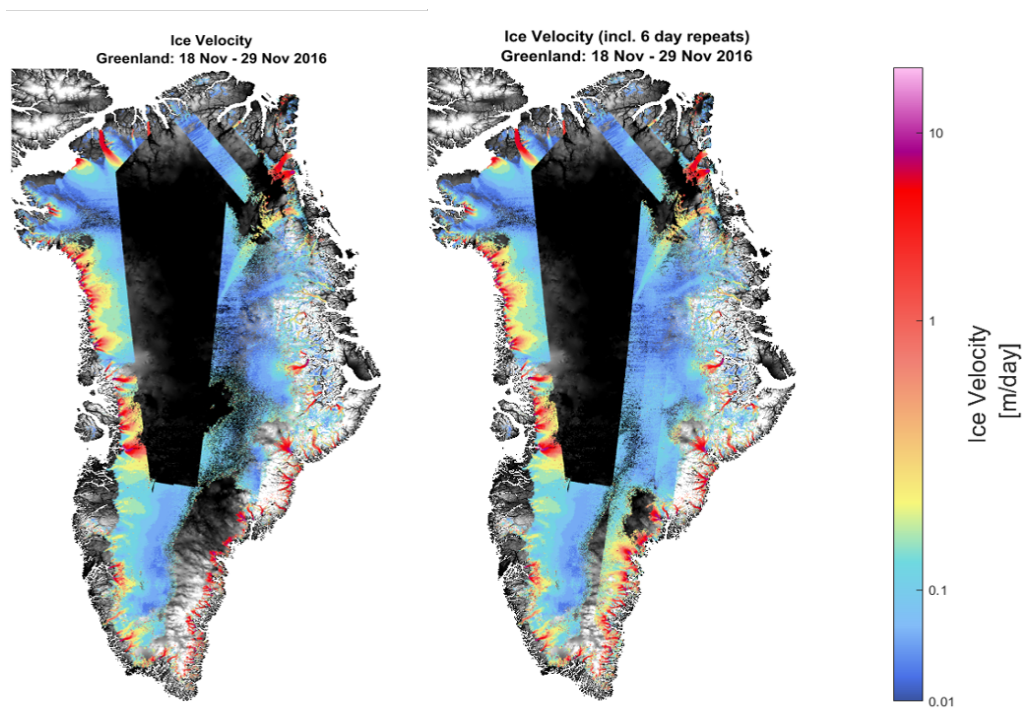

Figure 4: Examples of ice velocity maps for the Greenland ice sheet margin derived from ESA Sentinel-1 data. Left: Product produced by combining two repeat cycles from S1-A 12 days apart. Right: Same product improved by including a S1-B track covering the southeast coast, where offset tracking is inherently difficult due to significant changes of the surface. Background image is from Morlighem et al. (2014; 2015).

The two Sentinel-1 satellites repeat their tracks every 12 days, providing the unique opportunity to remotely monitor Greenland ice dynamics at an unprecedented six-day temporal resolution. Each ice velocity product is derived using data from two repeat cycles 12 days apart covering the Greenland ice sheet margin. As discussed in the paragraph below, the spatial coverage of the maps highly benefits from including 6-day repeats for some areas of the ice sheet margin, because the surface appearance often changes too much over 12 days for the off-set tracking to work. Thus, besides the 12 day repeats, the maps also include 6-day repeats for tracks 90, 112 and 141. The final maps are composites of all the processed data, and they thus span a 24-day period. A new map is produced every 6 days. The first map covers the period 14 September - 7 October 2016, and new maps become available as soon as the data is processed from www.promice.org.

The advantage of using SAR data is that data collection is affected neither by clouds nor the polar night. However, when the appearance of the surface changes too much between images for instance due to large snowfall, high melt rates or fast flow, it is no longer possible to track features between them. In southeast Greenland, all three processes combined make it inherently difficult to obtain complete ice velocity maps. Ionospheric disturbances also affect the quality

of the data product. Figure 4 shows how the spatial coverage of the ice velocity map is improved, when 6-day repeats are included for a track along the southeast coast of Greenland. Figure 5 gives an overview of how the quality and the spatial coverage of the maps vary over a year.
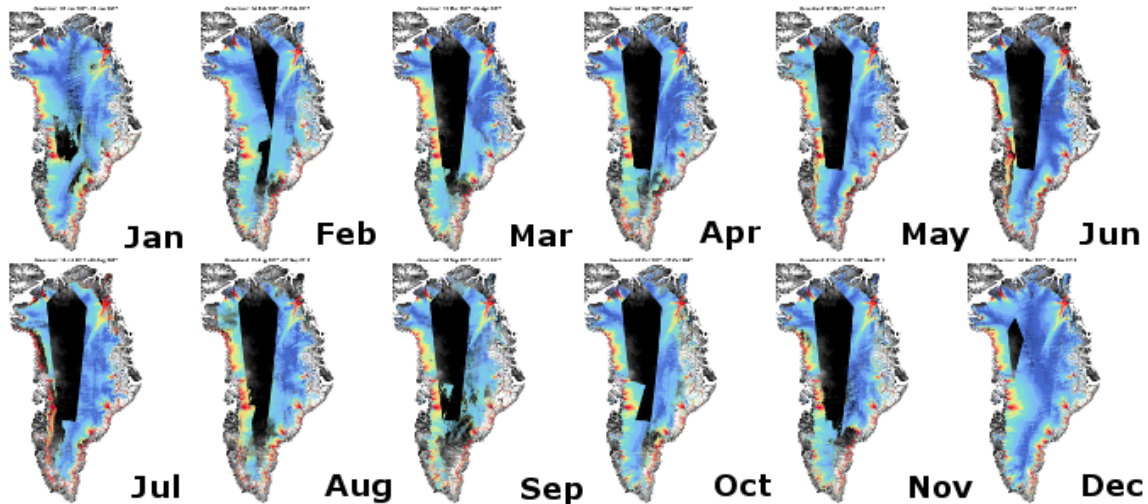

Figure 5: Examples of ice velocity maps each month in 2017.

2.4   FMI: SMOS soil frost

An updated soil freeze-thaw (F/T) product was developed based on ESA SMOS data and a new version of the product was generated. The F/T algorithm uses SMOS L3 daily gridded brightness temperature and calculates a frost factor (FF) from differences in brightness temperature (TB) at V and H polarization at 1.4 GHz: FF = (TBV-TBH)/(TBV+TBH). A threshold value, based on reference measurements of summer (thawed) and winter (frozen) measurements, is used for each SMOS pixel to determine soil state.

The product covers the Northern Hemisphere and is provided in 25 km x 25 km resolution EASE-Grid (see Fig. 6). The product is not yet publicly available, but will be made available in near future.
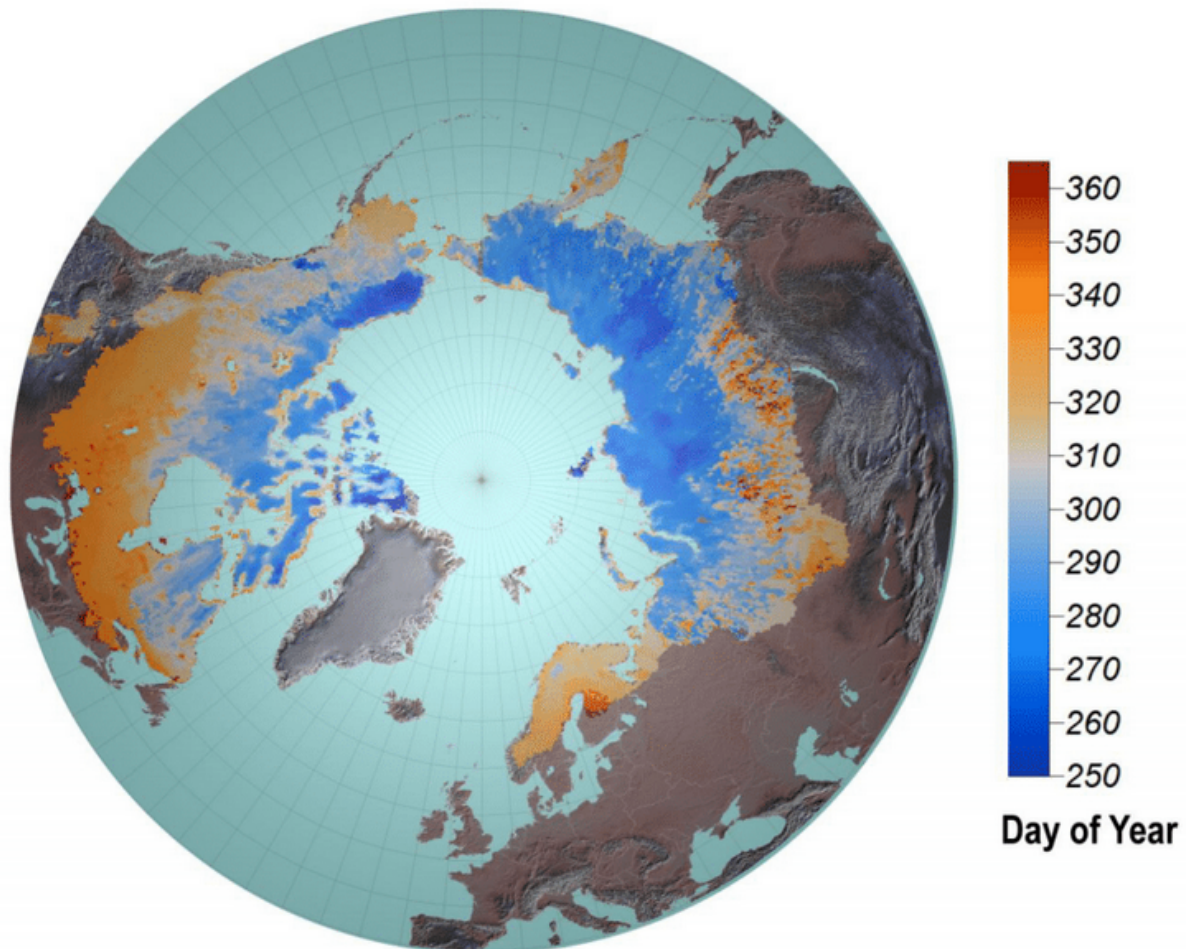
Figure 6: Day of freezing for the Northern Hemisphere in autumn 2015.

2.5   SMHI: Arctic Hydrological Cycle Observing System (Arctic-HYCOS)

The Arctic Hydrological Cycle Observing System (Arctic-HYCOS, www.whycos.org/whycos/projects/under-implementation/arctic-hycos) is an observation system under implementation by the National hydrological services (NHS) in Canada, Denmark, Finland, Iceland, Norway, Russian Federation, Sweden, and United States of America, in collaboration with The Global Runoff Data Centre (GRDC, www.bafg.de/GRDC) and the World Meteorological Organization (WMO, www.wmo.org). Arctic-HYCOS is intended to serve as a component of the World Hydrological Cycle Observing System network (WHYCOS, www.whycos.org), providing river discharge data from a network of hydrological stations operated by the NHS in the pan-arctic drainage basin of the Arctic Ocean and northern seas.

The Arctic-HYCOS river discharge data was assessed as described in D2.7 in relation to the objectives of the observation system, defined by the Arctic-HYCOS project steering committee:

- To provide data suitable for evaluating freshwater flux to the Arctic Ocean and northern seas, and

- To provide data suitable to study changes in Arctic hydrological regimes relative to climate change.

The Arctic-HYCOS dataset was enhanced with regard to temporal and spatial coverage by combination of data from GRDC and NHS repositories, and with regard to station metadata.

Arctic-HYCOS station network

The Arctic-HYCOS network is composed of stations from the regular observation networks, selected by the NHS for each country as suitable to fulfill the objective of the observation system. The stations are divided into two sub-networks:

- Hydrological regime stations covering the entire land mass draining into the Arctic Ocean and northern seas. There is no limitation to the size of land area drained; long term gauges are prefered but not necessary; ideally a wide geographical distribution is expected.
- Flow-to-ocean stations are the most downstream monitoring stations that would be used to estimate total river flow to the Arctic Ocean and northern seas. This is a subset of the Hydrological regime stations. Stations are limited to those greater than 5000 km2.

The current network includes 427 stations of which 72 are classified as part of the flow-to-ocean network (Fig. 7). This list was provided for the INTAROS assessment by the Arctic-HYCOS Steering committee (latest update 2018-05-12). The station list is still under revision by the Arctic-HYCOS project and is expected to be finalized and published at the GRDC website during 2018.
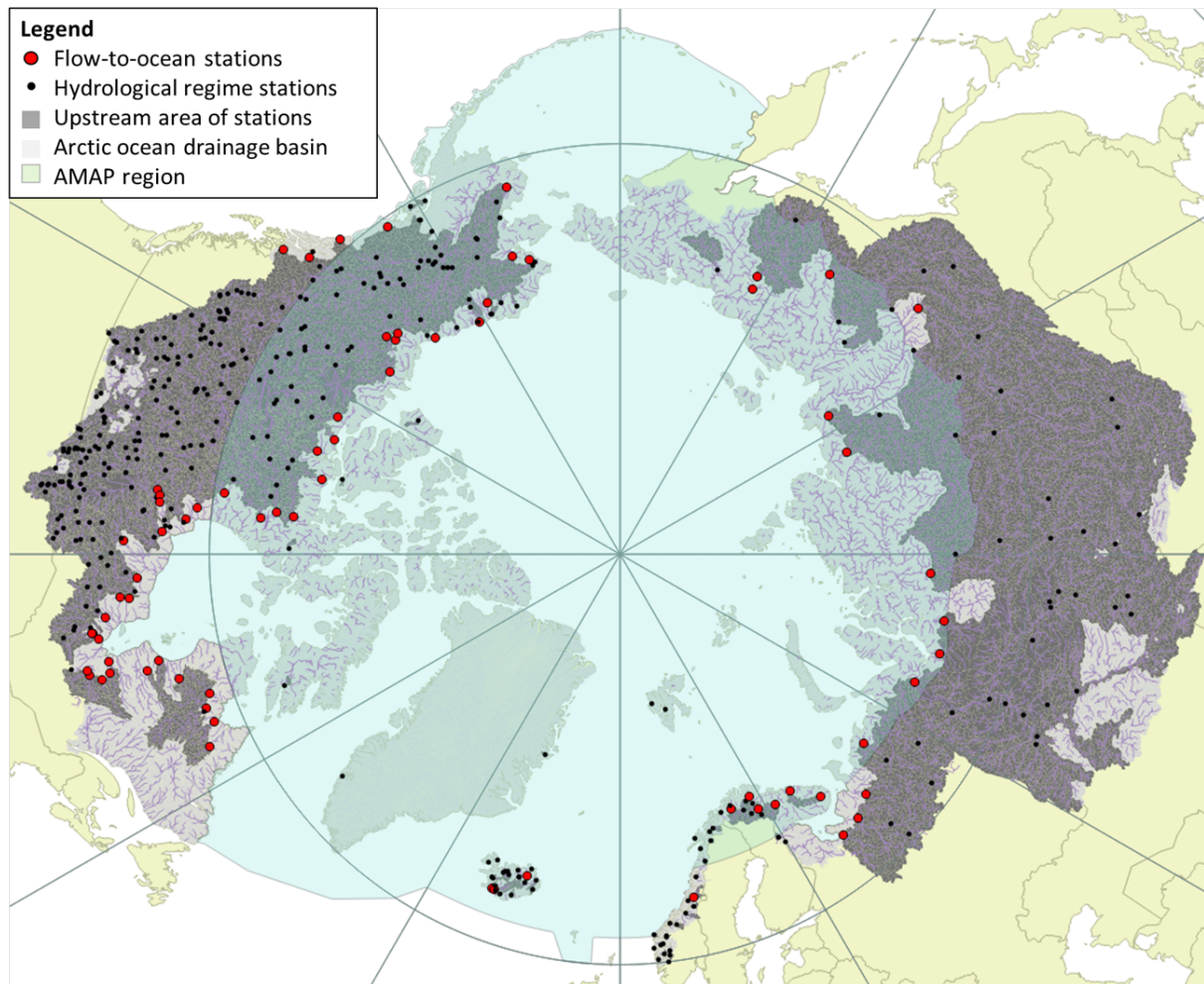
Figure 7: Drainage basin of the Arctic Ocean and related water bodies in the northern seas (light grey), the location of the Arctic-HYCOS stations and their upstream drainage basins (dark grey).

Enhancement of the Arctic-HYCOS station metadata

The Arctic-HYCOS station metadata contains the essential information about the station location (latitude, longitude), the area of the upstream drainage basin (km2), the station identifiers in the HYCOS, GRDC, and NHS data repositories, as well as station and river name, temporal coverage, sub-network (flow-to-ocean), and links to web-services providing realtime and historical data from the NHS if available. A spatial polygon defining the upstream drainage area, and a simplified quality flag will be implemented in the final version. The metadata definition was adopted from the WIGOS metadata standard for meteorological data (WMO, 2017), the GRDC metadata, and adapted to a minimum list of common attributes available from the different NHS.

River discharge is defined as the average flux of water (m3/s) through a cross-section of the river at the location of the river. However, this flux represents the aggregated hydrological response of the upstream drainage area of the river cross-section. A spatial polygon for the drainage basin of each station will be implemented as a required metadata to improve the interpretability and usability of the data. The current version of the Arctic-HYCOS metadata does not provide these polygons, and were left out from the current assessment. GRDC provides

on request drainage basin polygons derived from the HydroSHEDS elevation data available below 60°N. Assessment of these data versus nationally defined drainage basins, and basins derived from the high resolution Arctic-DEM data will be performed at a later stage.

Information related to instrumentation, validation and quality assurance procedures, originally measured data (water levels), transformation algorithms (so-called rating curves), scientific support, and technical readiness level is currently not provided by the Arctic-HYCOS or the GRDC metadata. To some extent, such information has been collected from the web services of the NHS.

Additional data used for the assessment and enhancement of the Arctic-HYCOS data

Additional information for the assessment and enhancement was taken from the global GRDC station list (), information compiled from the R-ArcticNet data (www.r-arcticnet.sr.unh.edu), as well as a network of sub-basin drainage basins delineated for the Arctic-HYPE model (hypeweb.smhi.se/arctichype), using a high resolution flow accumulation and elevaation data (90x90m) from the GWD-LR dataset (Yamazaki et al, 2013). Characterization of the geographical and landscape representation was further assessed by analysing overlay of the drainage basins with the land cover data (ESA CCI land cover), soil type (Harmonized World Soil Database) as prepared for the Arctic-HYPE model. A method for deriving the effective drainage area using the high resolution ArcticDEM elevation data was developed as part of the enhancement of the arctic-HYCOS station metadata.

Arctic-HYCOS river discharge data

Arctic-HYCOS river discharge time-series data with monthly and daily value were collected from several sources as summarized in Table 2:

- The GRDC Arctic-HYCOS database, which is available for free download as a compressed zip-archive. This archive currently contains data for 351 of the 427 stations latest updated 2017-12-31.
- The global GRDC data collection, including additional stations recently provided by the Arctic-HYCOS partners. Data available after request through a web-form.
- Data available from NHS services in Canada, USA, Finland through open web services.
- Data available from Iceland and Norway, available through email request.

The current Arctic-HYCOS metadata table includes GRDC identifier for 353 of 427 stations. Additionally 40 stations (in total 393) could be linked to the GRDC repositories using national stations identifiers and/or station location and upstream area. However, time-series data could only be found for 351 of these stations in the GRDC databases (obtained 2017-11-16). Time-series data for additionally 65 stations, including 7 flow-to-ocean stations, were obtained directly from the national hydrological services in Canada, USA, Finland, Iceland and Norway. Discharge data from 11 of the Arctic-HYCOS stations were not included, since these were added to the station list after the data collection for this assessment.

Country	N:o stations (flow to ocean)	N:o stations with data in GRDC Arctic-HYCOS subset	N:o stations with data in full GRDC database	N:o stations for which data was obtained from open National repositories	N:o stations missing from assessment	First and last years with data in GRDC database (total number of years)	Data accessibility on National Hydrological services
Canada	244 (39)	199 (32)	205 (33)	39 (6)	0 (0)	1892-2016 (119)	Web service with interactive download (scripted download not possible)
USA	60 (9)	36 (8)	37 (8)	23 (1)	0 (0)	1901-2017 (117)	Web service with open download
Russian Federation	61 (17)	61 (17)	61 (17)	0	0 (0)	1877-2015 (134)	No service
Greenland	2(0)	2(0)	2(0)	0	0 (0)	1996-2015 (94)	No service
Finland	8 (1)	1(1)	5 (1)	3	0 (0)	1921-2015 (94)	Web service with open download
Iceland	22 (3)	3 (2)	21 (3)	0	1 (0)	1932-2014 (83)	Web service with email request
Norway	30 (3)	5 (2)	20 (3)	0	10 (0)	1892-2015 (124)	Email request
Total	**427 (72)**	**307 (62)**	**351 (65)**	**65 (7)**	**11 (0)**	**1877-2017 (134**	

Table 2: Data sources for the assessment and enhancement of the Arctic-HYCOS river discharge data.

2.6 UPM: Methods to estimate glacier ice discharge to the ocean from in-situ and satellite observations

In Deliverable 2.7 we analyzed various observing systems, and associated data collections (see description in Section 2.17 of Deliverable 2.7), which we will use in Work Package 6.4 to develop a demonstrations of the iAOS for stakeholders. This demonstration will focus on the use of own and external in-situ and satellite data accessed through the iAOS to calculate the ice discharge to the ocean from selected Arctic tidewater glaciers, and to separate the frontal ablation into its two main components, namely glacier calving and submarine melting at the glacier front. In this section we describe the methods developed by UPM researchers with such aim. As the ice discharge data will be derived under WP 6.4, we do not include in Section 3 the data requirements (those of the source data have already been analyzed in Deliverable 2.7), nor an associated gap analysis in Section 4.

Frontal ablation, that is, mass loss by calving, subaerial frontal melting and sublimation and subaqueous frontal melting (Fig. 8, left panel), is an important component of the mass balance of tidewater glaciers and marine-terminating ice caps. It has been reported to account for up to 30-40% of the total ablation of some Arctic glacierized archipelagos and ice caps. Because of the difficulty of calculating separately the components of frontal ablation, it is usually approximated by the ice discharge through flux gates close to the calving fronts, calculated as the product of density, ice velocity and cross-sectional area (mass flux per unit time). If the considered flux gate is not close to the calving front, the surface mass balance between them should be taken into account. Possible front position changes and ice-thickness changes should also be taken into consideration.
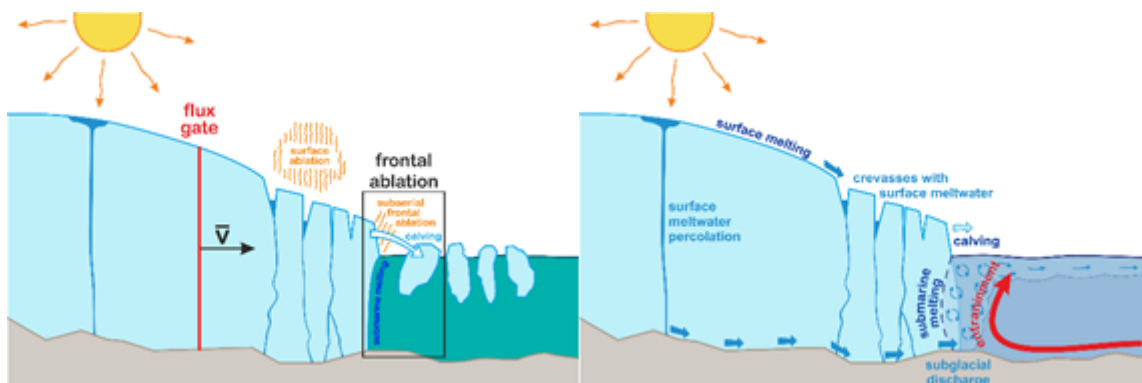

Figure 8. Left: main components of frontal ablation. Right: submarine melting at the glacier front.

A fundamental problem for estimating the ice discharge is that very often the cross-sectional area of tidewater glaciers is unknown. When only the thickness along the central flowline is known, U-shaped cross-sectional area approaches can be used. When no information at all (or little information) on ice thickness is available, inversion modelling can be used to infer the ice-thickness distribution from available data on glacier velocities, surface topography and mass balance, and glacier thinning/thickening. A further problem is that the usual error

estimates for ice discharge are very limited, most often based on rough estimates of upper and lower bounds for the error, rather than doing a statistical error analysis based on error propagation.

Within INTAROS, the UPM team has developed improved procedures for calculating the ice discharge from glaciers using the flux-gate approach and for improving their error estimates. Moreover, we have developed a method to quantify the partition of frontal ablation into its two main components, iceberg calving and submarine melting.

Regarding the estimate of glacier velocities from synthetic-aperture radar (SAR) Sentinel-1 data, Sánchez-Gámez and Navarro (2017) have developed a method, based on intensity offset tracking, for producing ice-surface velocity fields in range and azimuth directions from Sentinel-1 TOPS IW SLC Level-1 image pairs. The particularity of the procedure lies in the use of range offsets from ascending and descending passes, avoiding the use of azimuth offsets, since Sentinel-1 data shows a lower resolution in the azimuth direction. Simultaneously, we avoid the undesired ionospheric effect manifested in the data as azimuth streaks. The use of this novel approach has allowed us to obtain improved velocity fields with root-mean-square errors (RMSE) such as 0.012 m/day. Figure 9 illustrates the improvements provided by using this procedure.
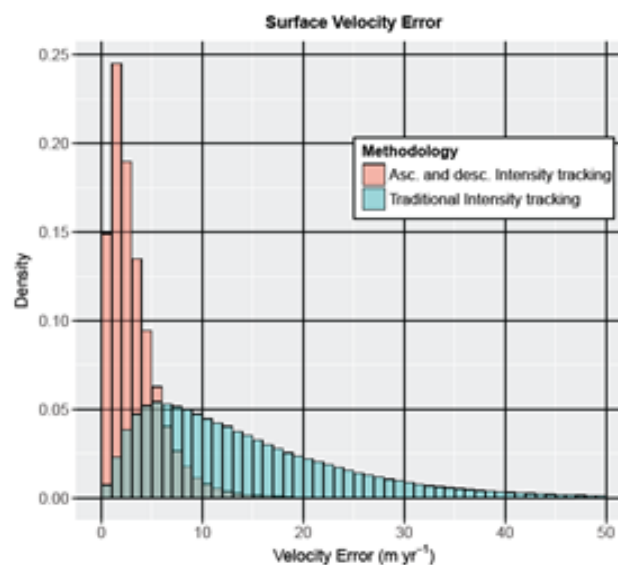

Figure 9. Errors in glacier velocity estimate from SAR data (from Sánchez-Gámez and Navarro, 2017).
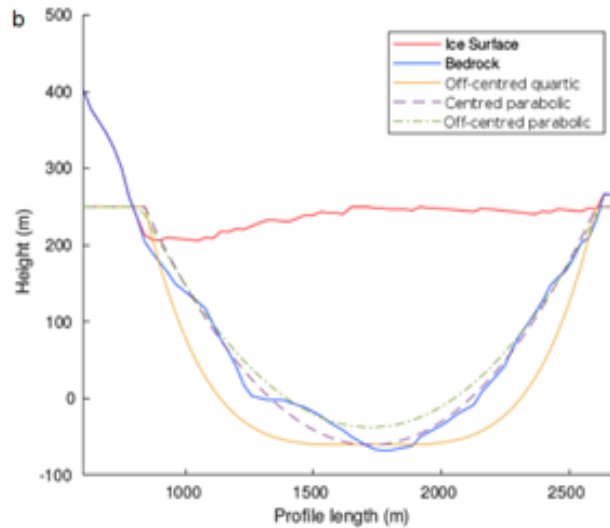
Figure 10. U-shaped cross-sectional profile approaches (from Sánchez-Gámez and Navarro, 2018).

In another paper, fully developed under the INTAROS framework, Sánchez-Gámez and Navarro (2018) have thoroughly analyzed, using error propagation, the various error components intervening in the error in ice discharge, and discussed procedures to minimize them. For glaciers with available GPR cross-sectional profiles, the total error in ice discharge is given by

$$\sigma_\phi = \sqrt{\sigma_{\phi_\rho}^2 + \sigma_{\phi_f}^2 + \sigma_{\phi_H}^2 + \sigma_{\phi_v}^2 + \sigma_{\phi_\alpha}^2} \; ,$$

where the various quadratic terms represent the contributions to the error due to the uncertainties in ice density, conversion factor from surface velocity to vertically-averaged velocity, ice thickness, velocity and angle between the glacier velocity vector and the vector normal to the cross-section used for the flux calculation. Each of these terms is of the form (taking one of them as example):

$$\sigma_{\phi_H} = \sqrt{\sum_i \left(\sigma_H \rho L_i f v_i \cos \alpha_i \right)^2} \; .$$

Their analysis shows that the velocity field is the dominant source of error for small glaciers with low velocities, while for large glaciers with high velocities the error in cross-sectional area becomes the main contributor to the total error. This stresses the interest of measuring ground-penetrating radar (GPR) cross-sectional profiles for the largest glaciers. They have also shown that glacier thinning/thickening between the times of SAR and GPR data acquisitions should not be disregarded, as it can imply a bias in the ice discharge estimate of up to ±8%. When GPR ice-thickness profiles are only available along (or close to) the central flowline of the glacier, Sánchez-Gámez and Navarro (2018) have developed a method to estimate the error in ice discharge when various U-shaped cross-sectional approaches are used (Fig. 10). They have shown that their proposed parabolic approach with axis displaced with respect to the GPR flight line generally performs better (low bias and admissible standard deviation) than the axis-centered parabolic approach usually employed in the literature. Finally, they have developed a

method to choose the optimal location of the U-shaped cross-section in terms of the along-flow variations of ice discharge, surface velocity and ice thickness.

Regarding the separation between the main components of frontal ablation, in another paper fully developed under the INTAROS framework, De Andrés et al. (2018) have designed a combined model of glacier dynamics and fjord circulation, in which the coupling between both models is accomplished through the calving and submarine melting. The glacier dynamics model uses the software Elmer/Ice to solve, using finite element methods, the Stokes problem governing glacier dynamics. The fjord circulation model, in turn, uses MITgcm software to solve, using the finite volume method, the Navier-Stokes system of differential equations (with Boussinesq approximation) governing the fjord circulation and Holland and Jenkins equations defining the thermodynamic equilibrium (salt and heat balance) at the fjord-glacier front interface. This coupled model allows to estimate the calving rates and the submarine melt rates (see Fig. 11 for melt rate estimates).
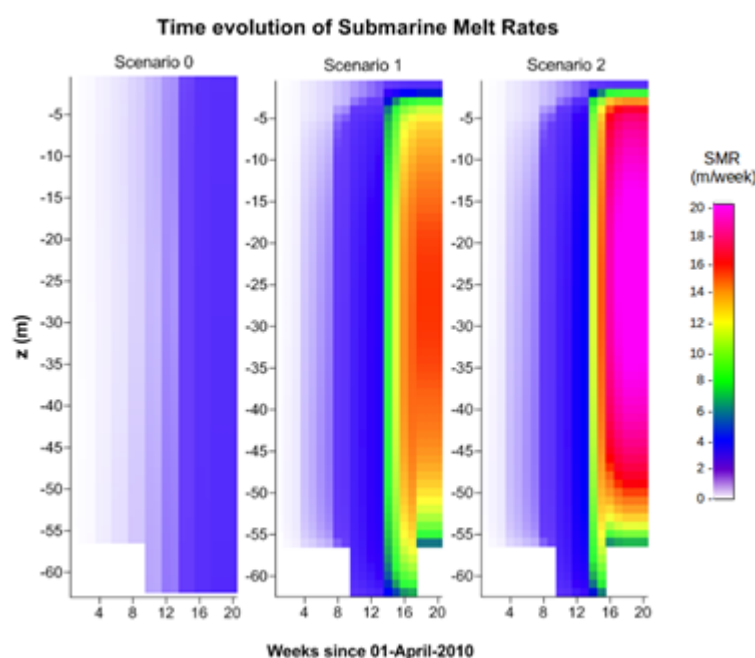

Figure 11. (from De Andrés et al., 2018) Evolution of submarine melt rates in Hansbreen calving front, Svalbard, under three different scenarios of subglacial discharge (see Fig. 8, right, for subglacial discharge).

Summarizing, the combination of the above-described methods provides a methodology to accurately estimate ice discharge from glaciers to the ocean and to quantify the partition of these mass losses between iceberg calving and submarine melt.

2.7 GFZ: Airborne observations of surface-atmosphere fluxes

As contribution to deliverable D2.8, GFZ calculated high resolution flux maps of methane (CH_4), carbon dioxide (CO_2), latent and sensible heat from two study areas in the Arctic. The study areas are the North Slope of Alaska and the Mackenzie Delta region in the Canadian

Arctic. The maps were derived from data from three flight campaigns (AIRMETH) that took place during the growing season of 2012, 2013 and 2016. The research aircraft Polar 5 of Alfred Wegener Institute (AWI) was used to quantify the surface-atmosphere exchange along horizontal flight tracks at about 40 m – 80 m above ground. Polar 5 was equipped with a Rosemount 5-hole probe attached to a nose boom for wind measurements and a greenhouse gas analyser of Los Gatos Research Inc. (2012: RMT-200; 2013 and 2016: FGGA 24EP) that was placed inside the cabin. The campaign setup and further instrumentation are described in more detail by Kohnert *et al.* (2014) for the 2013 campaign, in Hartmann *et al.* (2018) and in the INTAROS report associated with deliverable D2.7. The calculation of the fluxes is described in Kohnert *et al.* (2017) and the INTAROS report as well, and will be briefly summarized below followed by the description of the workflow resulting in two different varieties of flux maps. A schematic overview of the workflow is presented in Fig. 12.
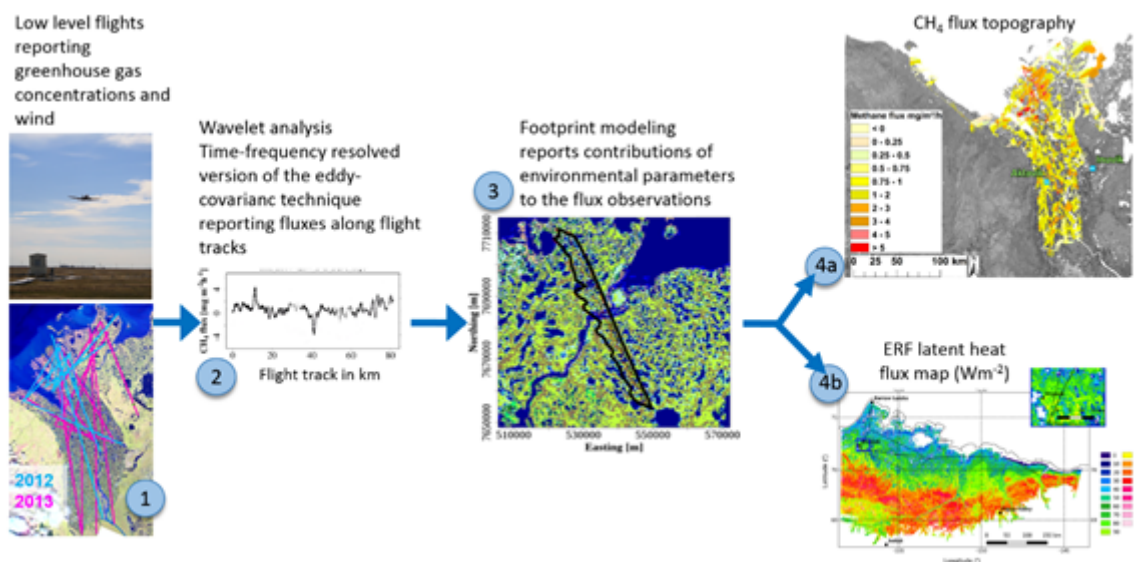

Figure 12: Workflow from flight campaigns (1), to flux calculation along each flight track via eddy-covariance technique (2), to footprint modeling (3), finally resulting in either (4a) flux maps that extent across the areas actually covered during the flights (Kohnert et al., 2017) or (4b) Environmental response functions (ERF) flux maps with fluxes projected beyond the actually covered areas using remote sensing and meteorological data (flux map adopted from Serafimovich et al., submitted).

Flux calculation

The fluxes of CH_4, CO_2, latent and sensible heat were calculated using an early version of the eddy4R software (Metzger *et al.,* 2017) via a time-frequency-resolved version of the eddy-covariance technique enabled through wavelet analysis (Metzger *et al.,* 2013). By moving a 1000 m long subinterval in steps of 100 m length along the flight lines, we obtained flux observations for every 100 m along a flight track. We obtained in-situ observed space-series of the exchange between surface and atmosphere at a spatial resolution of 100 m. Using a footprint model modified after Kljun *et al*. (2004) as described in Metzger *et al.* (2012) and Metzger *et al.* (2013), the fluxes were related to the respective surface influencing each measurement

during a flight. To obtain a regional flux information based on the "linear" fluxes along the flight tracks we used two approaches to calculate flux maps, to which we refer as i) flux topography and ii) ERF (Environmental Response Functions) flux map.

Flux map creation 1: Footprint flux map

Footprint flux maps (Fig. 13a) show the regional patterns of actually measured fluxes using the flux information along each flight track combined with the respective footprints and reproject the fluxes from the flight line to the area within the footprint using the weighted contribution from each area within the corresponding footprint. The weight of the contribution of each grid cell within the footprints depends on the distance from the measurement point, wind direction, and atmospheric stratification. Following a method suggested by Mauder *et al.* (2008) we derived the fluxes in each 100 m x 100 m grid cell using the sum of the products of the fluxes and footprint weights divided by the sum of footprint weights covering that grid cell

$$\frac{\sum_j^N \left(\sum_i^M f_{i,j} * g_{i,j} \right)}{\sum_j^N \left(\sum_i^M g_{i,j} \right)}$$

where n is the number of flux samples, i is the flux sample, X is the flux value, W the weight within the footprint, the weighted mean of the flux, is the mean weight. An example of an uncertainty map for the footprint flux map of CH_4 in the Mackenzie Delta is shown in Fig. 13b. For a scientific analysis of the data, we suggest to exclude grid cells with a standard error exceeding 30 %.
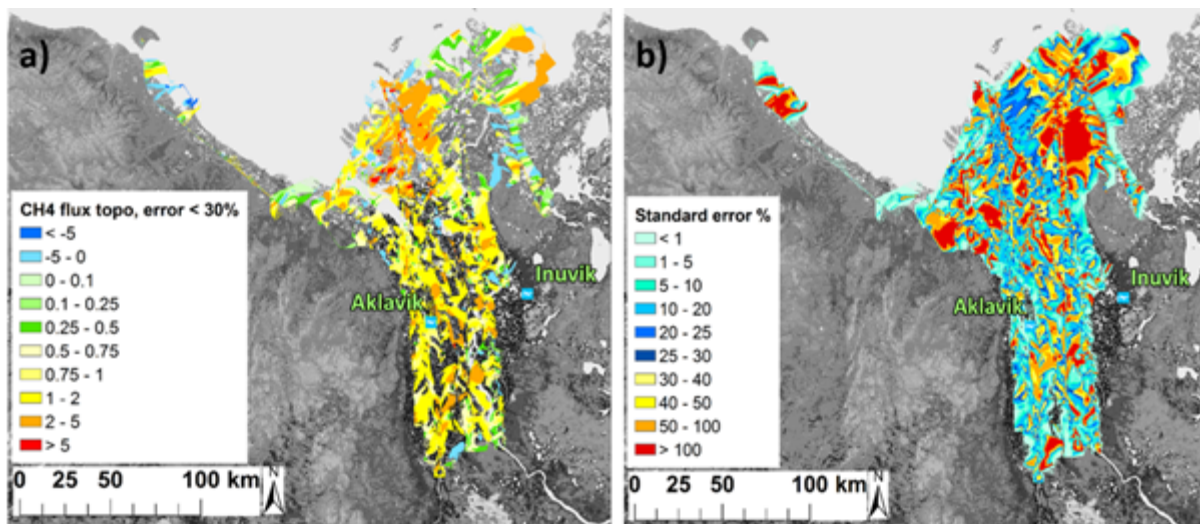

Figure 13: (a) Footprint flux map of CH_4 (modified after Kohnert et al., 2017) with CH_4 fluxes with standard error > 30 % removed and (b) map of standard error.

Flux map creation 2: Flux maps using Environmental Response Functions

The second type of flux map derived from the airborne flux measurements extends beyond the actual coverage of the measurements using environmental drivers of the fluxes to model flux maps for entire regions. The base for this flux calculation were the fluxes along the flight tracks

together with their corresponding footprints. Additionally, as described in Metzger *et al.* (2013), remotely sensed surface properties and meteorological model data were used as input parameters during the footprint modelling (cf. Metzger *et al.*, 2017) so that for each flux the information of the corresponding surface and meteorological properties within its corresponding footprint is stored.

Training

For each flux (CH_4, CO_2, sensible and latent heat) this information is used to train a boosted regression tree (BRT) model (Elith *et al.*, 2008; Metzger *et al.*, 2013), a machine learning technique, to learn relationships between environmental drivers such as vegetation indices or air temperature and the resulting flux. We call the dominant relations between environmental parameters and flux 'environmental response functions' (ERFs). The performance of the BRT is improved by combining numerous decision trees (Fig. 14).
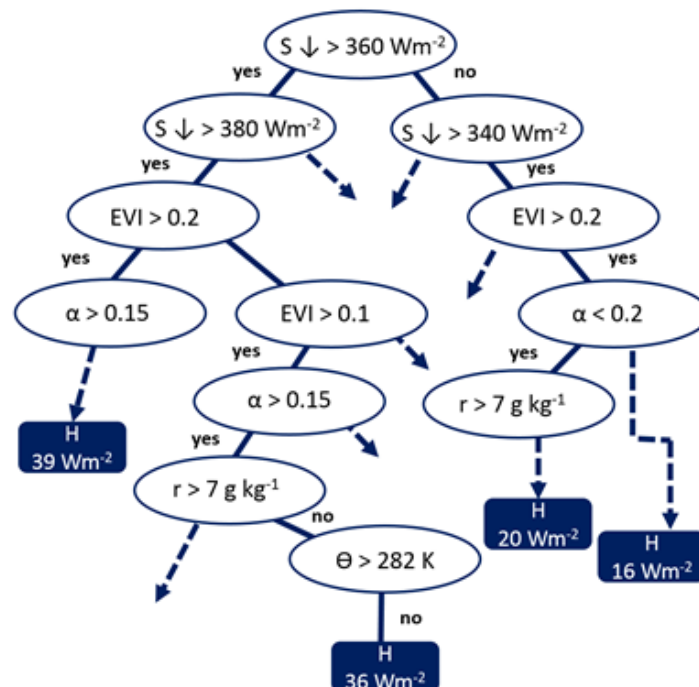

Figure 14: Exemplary decision tree of boosted regression trees for learning a response for the sensible heat flux H (modified after Serafimovich et al., submitted).

Map projection

The obtained ERFs are then used to project the fluxes to the entire area of interest (cf. Elith *et al.,* 2008; Metzger *et al.*, 2013), in our case the North Slope of Alaska and the Mackenzie Delta. To catch spatial variability of surface fluxes, the potential temperature, the dry mole fraction of water vapour, the shortwave down-welling radiation, and the height of the planetary boundary layer were simulated using the Weather Research and Forecasting (WRF) model and used as atmospheric drivers for the flux projection (Serafimovich et al., submitted). The fluxes are only projected into areas that are characterized by environmental states covered during the actual flights (Fig. 15 a and b). This results in gaps within the regional maps in areas characterized by, for example, air temperature that has not been measured during a flight. However, through the

extensive coverage with flight tracks, this method only results in very few gaps within the study areas. For each flux map, a complete uncertainty map could be derived as well. A list of environmental drivers used to calculate the map will accompany each flux map.
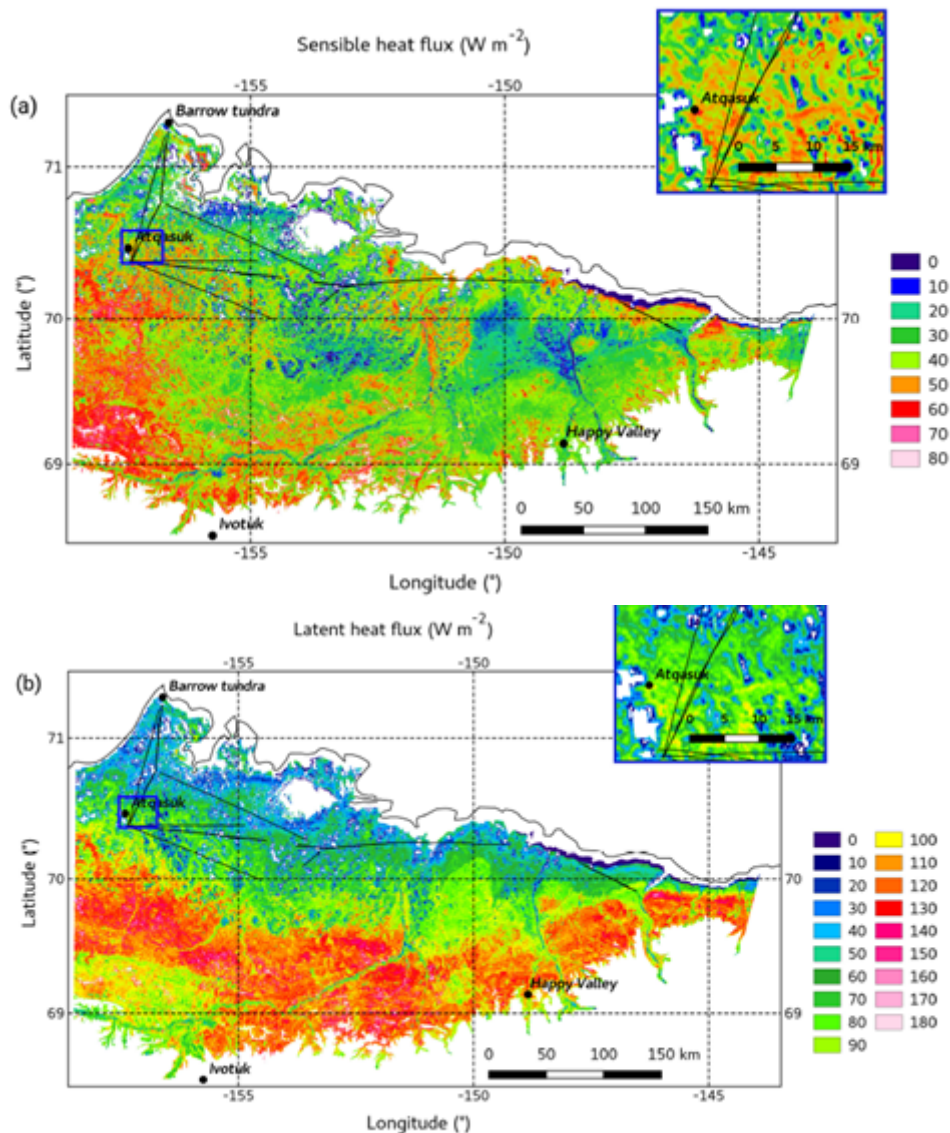

Figure 15: Exemplary flux maps of (a) sensible and (b) latent heat across the North Slope of Alaska derived from AIRMETH 2012 data. The maps are adopted from Serafimovich et al., submitted.

2.8   IGPAN

The Polish Polar Station Hornsund is located on the northern shore of the Hornsundfjord on Wedel Jarlsberg Land in SW Spitsbergen. Warm and humid air transported by extratropical cyclones from lower latitudes and warm West Spitsbergen current have significant influence on the climate, which is mild and maritime, with respect to its high latitude. The Hornsund meteorological station, established in July 1978 is located on a marine terrace at 10 m a.s.l., 300 m from the sea shore.

The first measurements of the ground thermal state in the vicinity of Polish Polar Station in Hornsund were initiated during the first Polish overwintering at Hornsund base in 1957/1958 and were continued in a few following summer seasons. Since July 1978 year round observations were renewed and are continued until now. Variations of ground thermal conditions have been measured routinely at four depths: 5, 10, 20, 50 cm and since the 1980s also at 100 cm. From the beginning of measurements, bent-stem soil thermometers at 5, 10, 20 and 50 cm and at 100 cm thermometer with a large time-scale constant in plastic pipe were used. In 2001, those bent stem thermometers were replaced by thermistor sensors Pt-100, that are less fragile, more reliable and collect the data every 1 minute. The only thermometer that remained is the one measuring ground temperature at 100 cm.

In the second half of August 2013, two new boreholes were established using a drilling rig on raised marine terraces, composed of marine sediments containing a mixture of sand and gravel with clay. Beneath 4–5 m thick marine deposits lies crystalline basement of metamorphic schists, paragneisses and marbles. The first borehole was located at the Hornsund meteorological site, the second 300 m to the east in a small (1.3 km²), nonglaciated Fuglebekken catchment, around 150 m from the shore of Isbjørnhamna. The installed thermistor chains were STG-073 with eight sensors (Pt-100 cl. 1/3B DIN 43760 with accuracy of 0.1°C), measuring temperatures at depths: 5, 10, 20, 50, 100, 150, 175 and 200 cm.

In spring 2017, three additional boreholes were established (borehole Brzydal 10 m deep with ground temperature observations at 0.2, 0.4, 0.8, 1.2, 1.6, 2.0, 2.5, 3.0, 3.5, 4.0, 5.0, 7.0, 9.0, 10.0 m by Geoprecision M-Log5W-DALLAS; borehole Lola 20 m deep with observations at the following depths: 0.2, 0.4, 0.8, 1.2, 1.6, 2.0, 2.5, 3.0, 3.5, 4.0, 5.0, 7.0, 9.0, 10.0, 11,0, 15.0, 18.0, 20.0 m by Geoprecision M-Log5W-DALLAS; borehole meteo station 12 m deep with observations at the following depths 0.2, 0.5, 1.0, 1.5, 2.0, 2.5, 3.0, 4.0, 5.0, 8.0, 10.0, 12.0 m by Vaisala QMT107 sensors PT100).

Since 1989, mass balance measurements and calculations of Hansbreen glacier located in the vicinity of Polish Polar Station Hornsund have been a part of a long term monitoring conducted by the station's staff. Work focuses primarily on the measurement of thickness and physical properties of the snow cover on the glacier. In the spring season, the snow density, size and type of crystals, compactness and humidity are measured and described in detail in the accumulation, ablation, and in the equilibrium zone of the glacier. Throughout the accumulation and ablation period, regular measurements of the thickness of snow and ice are carried out on 17 ablation stakes placed on the surface of the glacier and its tributaries. After taking into account the information from the snowpits, it allows calculation of the winter, summer and net surface balance of the glacier. Data related to mass balance monitoring are sent to the World Glacier Monitoring Service database (WGMS). Data on the mass balance of the Hans glacier, are systematically published in the "Fluctuations of Glaciers" and "Glacier Mass Balance Bulletin" issued by WGMS. At one of the ablation stakes in the ablation zone of the glacier (about 5 km from the forehead), continuous measurements of surface movement are conducted using a differential dGPS station. The positions (three components in the GPS differential system) of the other ablation stakes placed on the surface of the glacier are also regularly determined.

2.9   U Slaski: Front positions of tidewater glaciers in Hornsund (S Svalbard)

Front positions of tidewater glaciers in Hornsund are presented in the paper Błaszczyk et al. (2013); Fig. 16. The ice front position was examined for the following periods: 1899–1936–1960/1961–1976–1990–2001–2005–2010. For the period 1899–1990, we used several archival maps of varying accuracy, which was sometimes difficult to assess. All the topographical maps were digitally scanned, geocoded using ground control points and reprojected (when needed) into UTM33X system on the WGS 84 datum. For the period 1976–2010, we used optical and radar satellite images. The details on source and data accuracy are collected in the table "The front position changes" on the satellite orthophotomap enclosed to paper Błaszczyk et al. (2013).

For glacier extents in 1899, we used a scanned map (Wassiliew, 1925) from the Russian−Swedish expedition to Spitsbergen. During that expedition the meridian arch was surveyed and a triangulation network was established on the southern and eastern coasts of Spitsbergen. Despite the small scale (1:200 000) and low accuracy of cliffs positions on Vasiliev's map (~300 m), it is still valuable, due to lack of any other data from this time.

Glacier extents in 1936 were derived from topographic maps prepared and published by the Norsk Polarinstitutt (NP) in 1986–1994 at a scale of 1:100 000 based on oblique aerial photos taken in 1936–1938. The accuracy of these maps is very inhomogeneous and may vary from ten meters up to a few hundred of meters (H.F. Aas – 28 June 2011). Nevertheless, oblique photos from flights along the coastline are giving higher accuracy (~100 m) of ice cliff positions than for distant inland areas.

Front positions in 1961 for a few glaciers are plotted on the NP 1:100 000 map (C13 – Sørkapp, published in 1986). Due to revealed errors of front position of some glaciers for this period on the NP maps, in our study the cliffs lines in the western part of Hornsund Fjord in the 1960s were plotted using aerial photographs form the S60 and S61 series kindly provided by the NP. Fronts were measured photogrammetrically with Erdas software. For the rest of the region, topographical maps were used (Barna 1987).

The cliff positions based on the NP aerial campaign in 1990 were plotted on both the reedited series of NP maps (1:100 000) from 1986 and 1994, and on the maps issued in 2007 and 2008. Due to some discrepancies between both of editions, we checked fronts positions with the orthophotomap prepared for the Polish Polar Station area (Kolondra 2003 – unpublished data) on the basis of 1990's aerial photos kindly provided in digital form by the NP. Terminus positions were in accordance with the latest map edition (2007, 2008), therefore these maps were used to determine front positions of the tidewater glaciers in 1990 for the whole fjord.

Glacier extents in the period 1976–2010 were determined using satellite images: multispectral Landsat2 MMS (resolution 60 m), ALOS AVNIR (10 m, courtesy of Institute of Geophysics, Polish Academy of Sciences), ASTER (15 m), and panchromatic bands of Landsat−7 (15 m). Landsat images were freely acquired from the USGS EarthExplorer web page (http://earthexplorer.usgs.gov). Despite of the failure of Scan Line Corrector on ETM+ in May

2003, images were still usable for mapping glacier margins. For precise measurements of the dynamic changes of the glaciers, both orthorectified and non−orthorectified images needed geometrical correction in order to precisely map changes. We used the ALOS AVNIR image from 2009 (10 m resolution) as the reference image. In the first stage the ALOS AVNIR image was co−registered using the NP topographic maps 1:100 000 (2007, 2008), and then the other satellite images were co−registered to the ALOS AVNIR image. Generally, the same ground control points close to sea level were applied in the coregistration process.
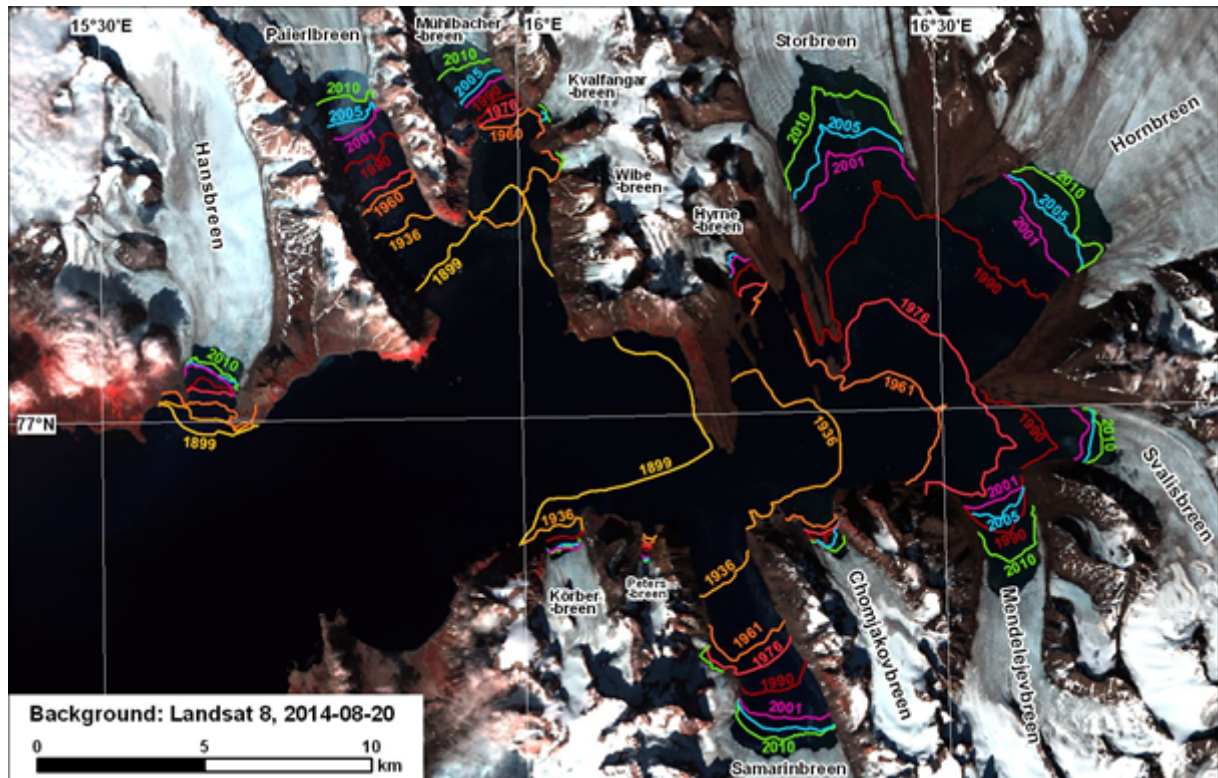

Figure 16. Post−LIA retreat of tidewater glaciers in Hornsund Fjord (after Błaszczyk et al. 2013, modified).

3. Literature

AON Design and Implementation Task Force, 2012, Designing, Optimizing, and Implementing an Arctic Observing Network (AON): A Report by the AON Design and Implementation (ADI) Task Force. Study of Environmental Arctic Change (SEARCH), Fairbanks, Alaska. 64 pp.

Atkinson, C., 2015: Ice Thickness Data, ERA-CLIM2 Deliverable D3.16, Report. http://www.era-clim.eu/ERA-CLIM2/Products/

Barna, S. (ed.), 1987: Topographic maps 1:25000, Institute of Geophysics Polish Academy of Sciences, Warsaw (based on aerial photos).

Błaszczyk, M., Jania, J.A. & Kolondra, L. 2013. Fluctuations of tidewater glaciers in Hornsund Fiord (Southern Svalbard) since the beginning of the 20th century. Polish Polar Research 34, 327–352.

Dall, J., Kusk, A., Nielsen, U., & Merryman Boncori, J. P. (2015). Ice Velocity Mapping Using TOPS SAR Data and Offset Tracking. *Proceedings of 9th International Workshop Fringe 2015*, 369–75

De Andrés, E., Otero, J., Navarro, F., Promińska, A., Lapazaran, J. and Walczowski, W. (2018). A two-dimensional glacier-fjord coupled model applied to estimate submarine melt rates and front position changes of Hansbreen, Svalbard. Submitted to J. Glaciol.

Eicken, H. et al., 2013: Dual-purpose Arctic observing networks: Lessons from SEARCH on frameworks for prioritization and coordination, White paper for Arctic Observing Summit, Vancouver, BC, Canada.

Ekström, G., M. Nettles, and A. M. Dziewonski, The global CMT project 2004-2010: Centroid-moment tensors for 13,017 earthquakes, Phys. Earth Planet. Inter., 200-201, 1-9, 2012. doi:10.1016/j.pepi.2012.04.002

Elith, J., Leathwick, J.R., Hastie, T. (2008) A working guide for boosted regression trees. *Journal of Animal Ecology,* **77**, 802-813.

GAIA-CLIM measurement maturity Matrix Guidance, 2015: Task 1.1: Report on system of systems approach adopted and rationale.

Gatz, D.F., Smith, L. (1995) The standard error of a weighted mean concentration – I. Bootstrapping vs other methods. *Atmospheric Environment*, **29**, 1185-1193.

Haimberger et al., 2015: Bias adjustments for radiosonde temperature, wind and humidity from existing reanalysis feedback, ERA-CLIM2 Deliverable 4.1, Report. http://www.era-clim.eu/ERA-CLIM2/Products/

Hartmann, J., Gehrmann, M., Sachs, T., Kohnert, K., Metzger, S. (2018) The Polar 5 airborne measurements of turbulence and methane fluxes during the AirMeth campaigns. *Atmospheric Measurement Techniques Discussions*, https://doi.org/10.5194/amt-2017-454.

Howat, I. M., A. Negrete, and B. E. Smith. 'The Greenland Ice Mapping Project (GIMP) Land Classification and Surface Elevation Data Sets'. *The Cryosphere 8*, no. 4 (2014): 1509–18.

International Seismological Centre, *Reference Event Bulletin*, http://www.isc.ac.uk, Internatl. Seismol. Cent., Thatcham, United Kingdom, 2018.

Kljun, N., Calanca, P., Rotach, M., Schmid, H. (2004) A simple parameterisation for flux footprint predictions. *Boundary-Layer Meteorology*, **112**, 503-523.

Kohnert, K., Serafimovich, A., Metzger S., Hartmann, J., Sachs, T. (2017) Strong geologic methane emissions from discontinuous terrestrial permafrost in the Mackenzie Delta, Canada. *Scientific Reports*, **7**, 5828.

Kohnert, K., Serafimovich, A., Hartmann, J., Sachs, T. (2014) Airborne Measurements of Methane Fluxes in the Alaskan and Canadian Tundra with the Research Aircraft „Polar 5". *Reports on Polar and Marine Research*, **673**, ISSN 1866-3192.

LFPMURCS: Low Frequency Passive Microwave User Requirement Consolidation Study. D-02 White paper on L-band radiometry for earth observation: status and achievements. ESA ITT AO/1-8731/16/NL/IA. In preparation.

Lee, O., H. Eicken, G. Kling, C. Lee, 2015. A Framework for Prioritization, Design and Coordination of Arctic Long-term Observing Networks: A Perspective from the U.S. SEARCH Program. ARCTIC VOL. 68, SUPPL. 1 (2015) http://dx.doi.org/10.14430/arctic4450.

Mauder, M., Desjardins, R.L., MacPherson, I. (2008) Creating Surface Flux Maps From Airborne Measurements: Application to the Mackenzie Area GEWEX Study MAGS 1999. *Boundary-Layer Meteorology*, **129**, 431-450.

Metzger, S., Junkermann, W., Mauder, M. *et al.* (2012) Eddy-covariance flux measurements with a weight-shift microlight aircraft. *Atmospheric Measurement Techniques*, **5**, 1699-1717.

Metzger, S., Junkermann, W., Mauder, M. *et al.* (2013) Spatially explicit regionalization of airborne flux measurements using environmental response functions. *Biogeosciences* **10**, 2193-2217.

Metzger, S., Durden, D., Sturtevant, C. *et al.* (2017) eddy4R 0.2.0: a DevOps model for community-extensible processing and analysis of eddy-covariance data based on R, Git, Docker, and HDF5. *Geosci. Model Dev.,* **10**, 3189-3206.

Morlighem, M., E. Rignot, J. Mouginot, H. Seroussi and E. Larour. 2014. Deeply incised submarine glacial valleys beneath the Greenland Ice Sheet, *Nature Geoscience*, 7:418–422. doi:10.1038/ngeo2167.

Morlighem, M., E. Rignot, J. Mouginot, H. Seroussi and E. Larour. 2015. IceBridge BedMachine Greenland, Version 2, Boulder, Colorado USA: NASA DAAC at the National Snow and Ice Data Center

Polar View, 2016. Polaris: Next Generation Observing Systems for the Polar Regions. D2.1 Gaps and Impact Analysis Report, ESA, pp 180.

Sánchez-Gámez, P. and Navarro, F. (2017). Glacier Surface Velocity Retrieval Using d-InSAR and Offset Tracking Techniques Applied to Ascending and Descending Passes of Sentinel-1 Data for Southern Ellesmere Ice Caps, Canadian Arctic. Remote Sensing, 9(5), 442 (doi: 10.3390/rs9050442).

Sánchez-Gámez, P. and Navarro, F.J. (2018). Ice discharge error estimates using different cross-sectional area approaches. A case study for Nunavut, Canada, 2016-2017. Submitted to J. Glaciol.

Serafimovich, A., Metzger, S., Hartmann, J., Kohnert, K., Zona, D., Sachs, T. (2018) Upscaling surface energy fluxes over the North Slope of Alaska using airborne eddy-covariance measurements and environmental response functions. *Submitted to Atmospheric Chemistry and Physics*.

Strozzi, T., Luckman, A., Murray, T., Wegmuller, U., & Werner, C. L. (2002). Glacier motion estimation using SAR offset-tracking procedures. *Ieee Transactions on Geoscience and Remote Sensing,* 40(11), 2384–2391

Wassiliew A.S. 1925. Océan Glacial arctique. Spitzberg. Région des travaux de l'expédition de l'Académies de sciences de Russie pour la mesure d'un arc de méridien en 1899–1901. Carte dresie d'aprčs les matériaux de l'expédition sous la rédactin de O.E. Stubendorff par A.S. Wassiliew. Échelle de 1:200 000.

WMO, 2015: List of all requirements. From OSCAR Observing systems Capability Analysis and Review Tool: https://www.wmo-sat.info/oscar/requirements

http://vocab.ndg.nerc.ac.uk/list/L201/current

https://science.nasa.gov/earth-science/earth-science-data/data-processing-levels-for-eosdis-data-products

--- END of DOCUMENT---

INTAROS

This report is made under the project
Integrated Arctic Observation System (INTAROS)
funded by the European Commission Horizon 2020 program
Grant Agreement no. 727890.

Project partners: